NANO LETTERS

pubs.acs.org/NanoLett

Letter

# Ultrafast Electron Cooling and Decay in Monolayer $WS_2$ Revealed by Time- and Energy-Resolved Photoemission Electron Microscopy

Yaolong Li, Wei Liu, Yunkun Wang, Zhaohang Xue, Yu-Chen Leng, Aiqin Hu, Hong Yang, Ping-Heng Tan, Yunquan Liu, Hiroaki Misawa, Quan Sun,* Yunan Gao,* Xiaoyong Hu,* and Qihuang Gong

Cite This: *Nano Lett.* 2020, 20, 3747−3753

Read Online

ACCESS | Metrics & More | Article Recommendations | Supporting Information

**ABSTRACT:** A comprehensive understanding of the ultrafast electron dynamics in two-dimensional transition metal dichalcogenides (TMDs) is necessary for their applications in optoelectronic devices. In this work, we contribute a study of ultrafast electron cooling and decay dynamics in the supported and suspended monolayer $WS_2$ by time- and energy-resolved photoemission electron microscopy (PEEM). Electron cooling in the Q valley of the conduction band is clearly resolved in energy and time, on a time scale of 0.3 ps. Electron decay is mainly via a defect trapping process on a time scale of several picoseconds. We observed that the trap states can be produced and increased by laser illumination under an ultrahigh vacuum, and the higher local optical-field intensity led to the faster increase of trap states. The enhanced defect trapping could significantly modify the carrier dynamics and should be paid attention to in photoemission experiments for two-dimensional materials.

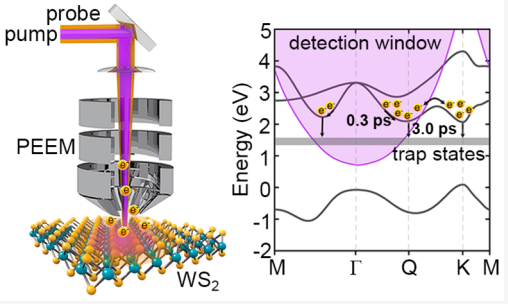


**KEYWORDS:** *electron cooling, defect trapping, transition metal dichalcogenides, ultrafast dynamics, photoemission electron microscopy, energy-resolved*

Two-dimensional transition metal dichalcogenides (TMDs) have drawn great attention, owing to their exotic properties, such as layer-dependent bandgaps,[1,2] large exciton binding energies,[3,4] valley polarizations,[5,6] and interlayer excitons.[7−9] TMDs have been reported as promising materials for applications in field-effect transistors, photodetectors, lasing,[10−12] etc. Understanding the charge carrier dynamics is not only crucial for all these applications but also fundamentally valuable. The two-dimensional limit and the reduced Coulomb screening make mono- and few-layer TMDs susceptible to external dielectric environments, adsorbates, structural defects,[13−15] etc. Among them, structural defects can be easily introduced during the material synthesis and device fabrication process or by exposing to electron beams, irons beams, and high-energy lasers,[16] which can strongly modify charge carrier dynamics.[17−21]

Ultrafast charge carrier dynamics has been characterized with the time scale ranging from tens of femtoseconds to hundreds of picoseconds, by using femtosecond transient absorption, time- and angle-resolved photoelectron spectroscopy (TR-ARPES), and time-resolved photoemission electron microscopy (TR-PEEM).[17−27] While it has been consistently reported that carrier thermalization occurs on a time scale of tens of femtoseconds,[24−26] following ultrafast charge carrier dynamics of carrier cooling, intervalley scattering, annihilation, and trapping have been reported with different values and different interpretations lacking consistency,[17−27] which could be due to the fact that different characterization and sample preparation methods were used. Obviously, more effort is required to reach a more comprehensive understanding of the ultrafast charge carrier dynamics in TMDs.

Here, we present an experimental study of the ultrafast electron dynamics in monolayer $WS_2$ by time- and energy-resolved PEEM. Electron cooling in the Q valley of the conduction band is clearly resolved on a time scale of 0.3 ps. We further show electron decay is mainly via a defect trapping process with a decay time of several picoseconds. In addition, the trap states are introduced by laser illumination during PEEM experiments, and the increase of trap states leads to faster electron decay. This phenomenon should be particularly paid attention to in photoemission studies with similar experimental conditions.

Figure 1a shows an optical image of the sample, which has three regions of monolayer $WS_2$ on a p-type Si (p-Si), on a 9 nm

**Received:** February 20, 2020
**Revised:** March 31, 2020
**Published:** April 3, 2020





https://dx.doi.org/10.1021/acs.nanolett.0c00742
*Nano Lett.* 2020, 20, 3747−3753

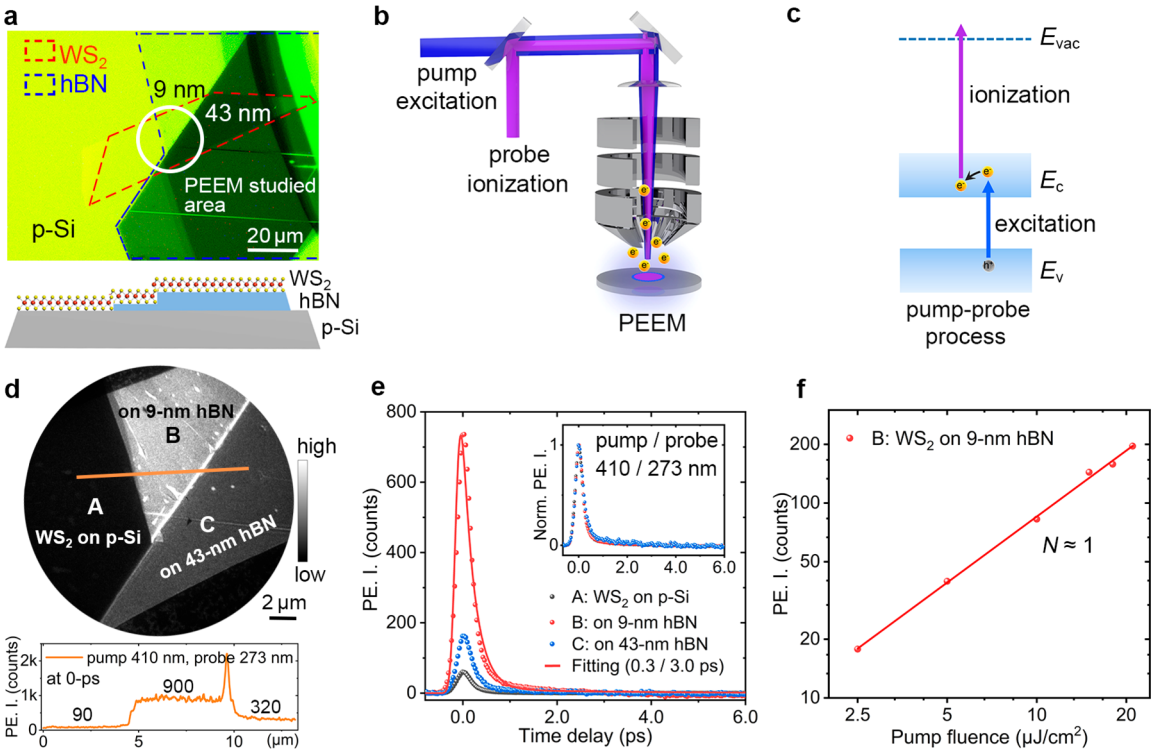


**Figure 1.** (a) Optical microscopy image and schematic of the supported $WS_2$ on p-Si and hBN; the white circle outlines the area studied by PEEM. (b) Illustration of the time-resolved PEEM measurement with pump and probe pulses at normal incidence. (c) Energy diagram of the pump−probe process. $E_v$, $E_c$, and $E_{vac}$ denote the valence band, conduction band, and vacuum level energies, respectively. (d) PEEM image at 0 ps time delay, in a field of view of 20 $\mu$m, with the pump pulse 410 nm (15 $\mu J/cm^2$) and the probe pulse 273 nm (0.5 $\mu J/cm^2$) at normal incidence. PE intensity along the yellow cross-cut line is shown at the bottom. (e) PE intensities (PE. I.) as a function of the time delay in the three regions. The decay trace for $WS_2$ on 9 nm hBN is fitted with a biexponential decay function. The normalized PE intensities are shown in the inset. (f) The pump−probe peak intensity as a function of the pump fluence for $WS_2$ on 9 nm hBN, obtained from a field of view of 10 $\mu$m.

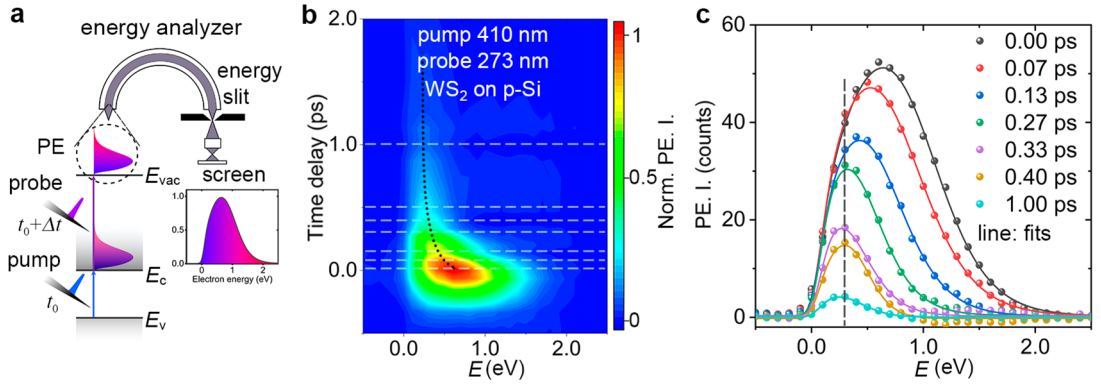


**Figure 2.** (a) Schematic of the time- and energy-resolved PEEM measurement. (b) Mapping of the PE intensity versus the energy and the time delay for the $WS_2$ on the p-Si with a pump wavelength of 410 nm. (c) Crosscuts from panel b and fits of the EDCs with Fermi−Dirac distributions.

hexagonal boron nitride (hBN), and on a 43 nm hBN. The principle of the PEEM measurement is illustrated in Figure 1b,c. A pump laser pulse with a tunable wavelength in visible range excites electrons from the valence band to the conduction band, and in following, a probe laser pulse with a wavelength of 273 nm (4.54 eV) ionizes the photoexcited electrons into a vacuum. By tuning the time delay between the pump and probe pulses, the electron evolving dynamics can be temporally resolved. Figure 1d presents a typical PEEM image in a field of view of 20 $\mu$m with the pump pulse 410 nm (15 $\mu J/cm^2$) and the probe pulse 273 nm (0.5 $\mu J/cm^2$) at the zero-time delay, and Figure 1e shows the photoemission (PE) intensity decay traces. A linear dependence between the PE intensity and the pump fluence is observed (Figure 1f), meaning the excitation is via the single-photon absorption process. We note that the charge carrier dynamics in this study are only for electrons excited to the conduction band, since only these electrons are ionized and detected. The pump−probe signals are dominantly from the monolayer $WS_2$, and the signals from the underlying p-Si are negligible (see Figure S9).

A large difference of PE intensity in the three regions is seen in Figure 1d,e and is due to the different local optical-field intensity of both the pump and probe pulses on the $WS_2$ layer, induced by the optical interference effect, which has been simulated using finite-difference time-domain (FDTD) simulations. From the simulations, the optical-field intensity of both the pump and


https://dx.doi.org/10.1021/acs.nanolett.0c00742
Nano Lett. 2020, 20, 3747−3753

probe lights varies periodically with the thickness of the hBN layer (Figure S7). The simulation results are sensitive to the parameters used, e.g., the thickness and refractive index of hBN and nonlinear order of PE, and could result in the discrepancy between the simulated and experimental results. Despite the large difference in PE intensity in the three regions, we found that the normalized PE intensity traces are nearly identical, as shown in the inset of Figure 1e. The PE intensity traces can be fitted by biexponential decay convoluted with the instrument response function (Figure S8), and the two components of decay time with 0.3 and 3.0 ps are determined. Notably, the normalized PE intensity traces are independent of the pump fluence (Figure S10).

To reveal the charge carrier decay dynamics, we measured the evolution of electron energy distribution in energy and time. As schematically illustrated in Figure 2a, the electrons are excited by the pump pulse and form an energy distribution in the conduction band. After a time delay $\Delta t$, they are ionized by the probe pulse and imaged by the energy analyzer. Figures 2b depicts the energy distribution and intensity evolution of the photoexcited electrons in energy and time from the region of $WS_2$ on p-Si. Figure 2c shows the electron energy distribution curves (EDCs) at different delay times along the dashed cross-cut lines in Figure 2b. Similar results are observed in the other two regions (Figure S11).

Figure 2c depicts that, in the beginning, 0.3 ps, the electron energy distribution exhibits a rapid peak shift toward lower energy along with the amplitude decrease. The peak shift directly reflects that electron is cooling from higher energy levels to lower ones. After approximately 0.3 ps, the peak shift stops, and only an amplitude decrease can be observed, indicating that electron cooling has completed. The electron energy distribution can be fitted with a Fermi−Dirac distribution $f(E, E_F^*, T_e)$ multiplied by the local density of states $g(E)$ and convoluted with the Gaussian instrument response function $G(\Delta E)$.[28] The PE intensity as a function of energy obeys the equation $\mathrm{PE}(E) = A\sqrt{E - E_c}(\exp(E - E_F^*)/k_B T_e) + 1)^{-1} \otimes G(\Delta E)$, where $E$ is the electron energy, $E_c$ is the conduction band edge, $E_F^*$ is the Fermi level, $k_B$ is the Boltzmann constant, $T_e$ is the electronic temperature, and $\Delta E$ is the energy resolution of 150 meV. The fitted electronic temperature is initially at 2800 K and drops to 1500 K after 0.3 ps, meaning hot electron cooling. We use the electronic temperature to characterize hot electron distribution in Figure 2b,c because carrier thermalization from the initial nonequilibrium electron distribution occurs on a time scale of tens of femtoseconds, much shorter than the excitation pulse duration of 120 fs. The energy-resolved PEEM measurements were also performed with the pump wavelength of 590 nm, and similar results are observed, except that the hot electron populations have a lower energy (Figure S13).

Further analysis of the electron decay process requires first to know where in the energy band the electrons can be excited and detected. We calculated the band structure, the band gap, and the gradient of the band gap to the momentum (Figure 3a,b), following the three-band tight-binding model.[29] Under excitation with 410 nm (3.0 eV) photons, the K valley is certainly populated with hot electrons. Besides, because of the band nesting,[30,31] electrons can be excited to the left side of the Q valley (Figure 3a,b) with energy higher than that at the Q point, and a few electrons may also be excited to the valley between the Γ and M point. For our TR-PEEM measurement, due to the energy and in-plane momentum conservations, the 273 nm (4.54 eV) photons can only ionize electrons with a

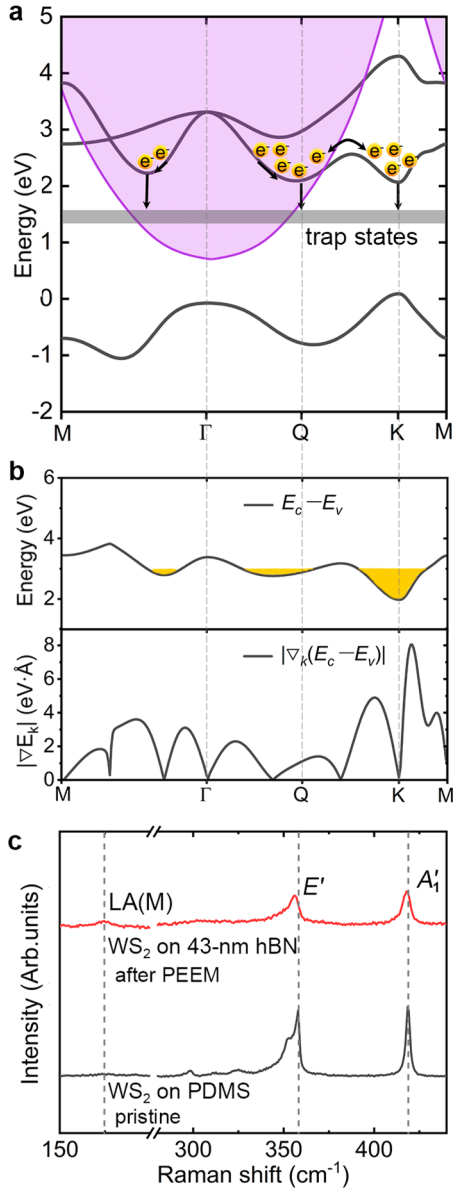


**Figure 3.** (a) Energy band diagram for monolayer $WS_2$ and the processes of carrier dynamics after photoexcitation with the pump wavelength of 410 nm. The purple-colored region denotes the PE detection window of the probe pulse. The observed processes by TR-PEEM are attributed to electron loss in the PE detection window. (b) The difference of $(E_c - E_v)$ (upper panel) and modulus of its gradient (lower panel) for monolayer $WS_2$. (c) Raman spectra for the supported $WS_2$ after PEEM measurements and the pristine $WS_2$ on PDMS.

momentum smaller than $k_{\parallel}$ determined by the equation $\hbar k_{\parallel} = \sqrt{2m(h\nu - E_b - \phi)}$, where $h\nu$ is the photon energy, $E_b$ is the binding energy, and $\varphi$ is the work function. Figure 3a shows the calculated detection window of the probe pulse by the color-coded region, which indicates the PE intensities are mainly due to electrons ionized from the Q valley, and the energy zero in the EDCs is likely at the conduction band edge of the Q valley.

From Figure 3a, it is clear that the electron cooling observed in Figure 2 occurs mainly in the Q valley and completes in 0.3 ps. Based on the band structure (Figure 3a,b), the hot electrons are partially generated directly in this valley and possibly partially coming from the K valley.[26,27] Intervalley hot electron transfer is evidenced by the similar results as in Figure 2b,c under 590 nm


https://dx.doi.org/10.1021/acs.nanolett.0c00742
Nano Lett. 2020, 20, 3747−3753

(2.10 eV) excitation, in which case the photons cannot directly excite electrons in the Q valley (Figure S13).

The decrease of PE intensity, composing two components, reflects electron loss from the detection window, and several decay paths are possible, such as intervalley transfer, Auger recombination, electron transfer to the substrate, and trapping. The intervalley transfer from the Q to the K valley, i.e., leaving out of the detection window during the cooling process, is highly possible, since we have observed its reverse process of hot electron transfer from the K valley to Q valley (Figure S12 and Figure S13). The electron intervalley transfer has been reported by some groups.[26,27] However, we cannot prove or exclude this possibility. Momentum-resolved PEEM and a higher photon energy are required for future studies. Auger recombination involves multiple charge carriers and is sensitive to the pump fluence.[22,23] We found that the normalized decay traces overlapped for different pump fluences and can exclude this decay path (Figure S10). Electron transfer to the substrate would be sensitive to the hBN thickness and is conflicting with our observation (Figure 1e). Additional experimental results presented later on the suspended $WS_2$ can firmly exclude this decay path. Therefore, we propose that the trap states play a significant role in the observed electron loss.[17−19] Particularly, we noticed that the slower decay component in the PE intensity trace became faster with accumulated measurement time (Figure S12). We suspect that the PEEM measurements gradually lead to more trap states forming. Since the cooling time is identical to the fast component of decay time, we attribute the fast decay component to hot electron decay including two possible paths of intervalley transfer and to trap states and interpret that the slow component is dominantly owing to the cooled electron decaying to trap states.

As additional evidence for trap states forming, we noticed that the photoluminescence (PL) was totally quenched after PEEM measurements (see Figure S2 and more samples without PEEM measurements in Figure S3). To characterize the sample change, we measured the Raman spectra for a pristine monolayer $WS_2$ and that after PEEM measurements. In Figure 3c, there are two intense peaks located at ∼357 $cm^{-1}$ and ∼419 $cm^{-1}$, which can be assigned to the $E'$ and $A_1'$ modes, respectively, based on the symmetry of monolayer $WS_2$.[32] After PEEM measurements, a red shift in frequency and an asymmetric broadening toward lower frequency were observed for both $E'$ and $A_1'$ modes because of the quantum confinement effect. Moreover, the LA (M) mode became stronger relative to the intensity of $E'$ and $A_1'$. It has been reported from several studies that these features are closely related to structure defects,[33−35] which can introduce midgap electron trap states and quench photoluminescence.[33−38] These results support our interpretation of trap states contributing significantly to the ultrafast electron loss from the conduction band.

To additionally check our entire interpretation, we fabricated a sample with a monolayer $WS_2$ on a Si substrate with empty holes, as shown in Figure 4a. The monolayer $WS_2$ was mechanically exfoliated and transferred onto the substrate. The hole has a diameter of 7 $\mu$m at the top and a height of about 3 $\mu$m and a bow-shaped bottom (Figure 4a). Typical PEEM images from the suspended $WS_2$ are shown in Figure 4b, obtained from a field of view of 10 $\mu$m, with a pump pulse of 410 nm (5 $\mu J/cm^2$) and a probe pulse of 273 nm (0.1 $\mu J/cm^2$). The top and bottom images are the same, except that the contrast is adjusted to show the details in the brightest region. The strong PE spot in the center is due to the optical focusing effect from the bow-shaped bottom. The PE intensity decreases from the center to the edge, and Figure 4c shows the PE intensity change along the cross-cut line in Figure 4b.

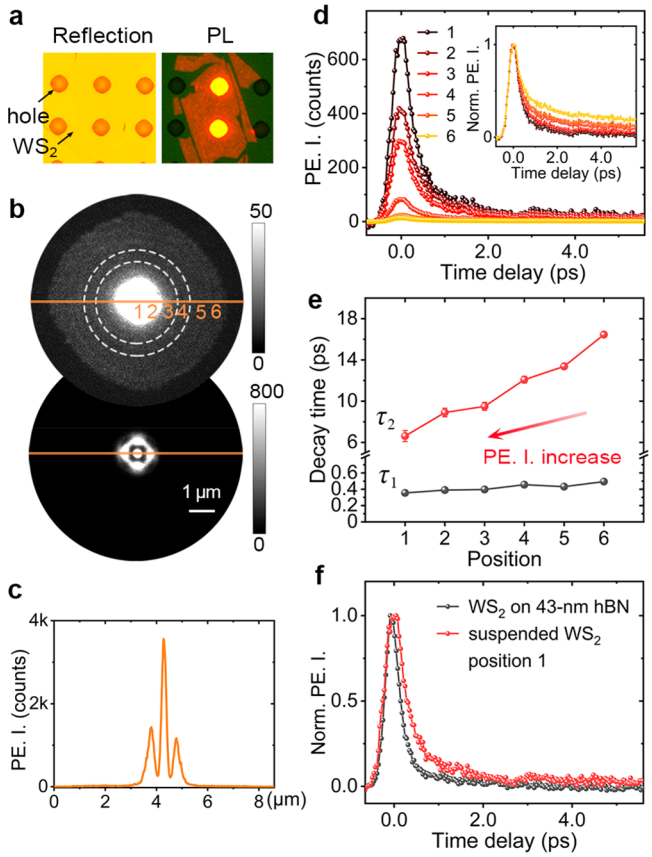


**Figure 4.** (a) Optical microscopy images, including reflection contrast (left) and PL signals (right), for the monolayer $WS_2$ on a silicon substrate with holes. (b) PEEM images at 0 ps time delay with the pump pulse 410 nm (5 $\mu J/cm^2$) and the probe pulse 273 nm (0.1 $\mu J/cm^2$) at normal incidence. The upper and lower images are the same, except that the contrast is adjusted to show the details in the brightest region. Six annular regions from the center to the edge are marked. PE intensity along the yellow cross-cut line is shown in panel c. (d) PE intensity traces and the normalized ones for the six regions. (e) The fast and slow components of decay time for the six regions. (f) Comparison of the decay traces for the supported and suspended $WS_2$.

The PE image is then divided into six annular regions from the center to the edge to investigate the carrier dynamics (Figure 4b), and the corresponding PE intensity traces are shown in Figure 4d. The extracted decay times for the six regions are shown in Figure 4e. It can be seen that the decay time of the fast component is nearly independent of PE intensity, while the decay time of the slow component decreases with the increase of PE intensity. It is needed to clarify that the dynamic change is not due to the pump or probe−fluence difference, since we have checked that the measured dynamics were independent of fluence in a short time (Figures S14 and S15, see also Figure S16 for probe−fluence dependence). Instead, we attribute this observation to the photon-induced increase of the trap states, as same as what has been observed on the supported monolayer $WS_2$, where the accumulation of measurement time has led to the same trend (Figure S12). Apparently, the increase of trap states correlates to the intensity and time of being exposed to the pump−probe photons. Additionally, a typical decay trace on the suspended $WS_2$ is similar to the trace on the $WS_2$ supported by


https://dx.doi.org/10.1021/acs.nanolett.0c00742
Nano Lett. 2020, 20, 3747−3753

43 nm hBN (Figure 4f). All these results strongly suggest that the slow decay component is dominantly owing to electrons decaying to trap states.

After PEEM measurements, we also observed that the PL signals were strongly reduced on the suspended $WS_2$ (Figure S2), and similar defect features appeared in the Raman spectra (Figure S4). From this sample, a weak but measurable defect-bound exciton peak (at ∼660 nm, 1.88 eV) appeared in the PL spectra (Figure S2). These results imply that the trap states are defects of S-vacancies,[19,39] which might be formed slowly by S-escaping under high energy photon illumination in an ultrahigh vacuum (see Figure S5 for the passivation of S-vacancy by oxygen adsorption and more discussions on defects in the Supporting Information).

In conclusion, we present a study of ultrafast electron cooling and decay dynamics in the supported and suspended monolayer $WS_2$ by time- and energy-resolved photoemission electron microscopy (PEEM). Electron cooling in the Q valley of the conduction band is clearly resolved in energy and time, on a time scale of 0.3 ps, and hot electron intervalley transfer is also observed indirectly. Electron decay is mainly via a defect trapping process with a decay time of several picoseconds. The trap states can be produced and increased by laser illumination under an ultrahigh vacuum, and the higher local optical-field intensity increases the trap states faster. The increase of trap states leads to faster electron decay and photoluminescence quenching. This study reveals the role of defect trapping in photoemission measurements for two-dimensional materials, and more effort is required to investigate their intrinsic properties with PEEM.

**Materials and Methods.** *Sample Fabrication and Characterization.* $WS_2$ and hBN flakes were mechanically exfoliated on polydimethylpolysiloxane (PDMS) sheets from bulk crystals (HQ graphene) and then transferred to the p-Si substrate layer-by-layer by using the all-dry transfer method.[40] The $WS_2$ monolayer was characterized by photoluminescence and Raman spectra and atomic force microscopy (AFM). The thicknesses of hBN flakes were measured by AFM. The holes on Si substrate were fabricated with conventional photolithography and inductively coupled plasma etching. All samples were annealed under an ultrahigh vacuum (approximately $10^{-9}$ Torr) at 300 °C for 2 h before loading into the PEEM chamber.

*PEEM Measurement.* The PEEM measurements were performed by using a high-resolution low-energy electron microscopy (LEEM)/PEEM system (ACSPELEEM III, Elmitec GmbH) equipped with an aberration corrector and imaging energy analyzer. A commercial Ti:sapphire femtosecond laser (Mai Tai HP, Spectra-Physics, pulse duration: 80−100 fs) operated at 820 nm with a repetition rate of 80 MHz and output power of 2.9 W was used as the laser source to pump an optical parametric oscillator (OPO) (Inspire Auto 100, Spectra-Physics). The SHG port (410 nm, ∼1 W) and signal light port (490−750 nm, maximum power: 350 mW) of the OPO were used to provide pump pulses, while third-harmonic-generation signals (273 nm, ∼10 mW) from a residual fundamental laser (820 nm, ∼1.1 W) were used as the probe pulse for the time-resolved PEEM measurements. The time resolution of the pump−probe system was approximately 200 fs, evaluated by cross-correlation measurements, while the pulse duration of an individual fundamental laser after passing through the optical path was approximately 120 fs, measured by frequency-resolved optical gating (FROGscan MP-001.CX, MesaPhotonics). The pump and probe pulses were focused on the sample surface at normal incidence to spot diameters of approximately 180 and 100 μm, respectively. The energy-resolved PEEM measurements were performed in imaging mode by inserting a 12.5 μm energy slit and sweeping the start voltage in a step of 0.1 eV to allow electrons with different energies through the energy slit. The time-dependent EDCs were obtained by using energy-resolved images at a series of time delays between the pump and probe pulses. The PE intensity decay traces and EDCs were plotted by subtracting the background PE signals before the pump−probe zero point.

## ■ ASSOCIATED CONTENT

### Supporting Information

The Supporting Information is available free of charge at https://pubs.acs.org/doi/10.1021/acs.nanolett.0c00742.

AFM image of the supported $WS_2$; PL and Raman characterizations; FDTD simulations on optical interference effect; time resolution of the TR-PEEM measurements; PEEM measurements for the supported $WS_2$; PEEM measurements for the suspended $WS_2$ (PDF)

Movie S1 (MP4)

## ■ AUTHOR INFORMATION


### Corresponding Authors

**Quan Sun** − *Research Institute for Electronic Science, Hokkaido University, Sapporo 001-0021, Japan*; orcid.org/0000-0001-5413-8038; Email: quansun@es.hokudai.ac.jp

**Yunan Gao** − *State Key Laboratory for Artificial Microstructure and Mesoscopic Physics, School of Physics, Peking University, Beijing 100871, China; Frontiers Science Center for Nano-optoelectronics & Collaborative Innovation Center of Quantum Matter, Beijing 100871, China; Collaborative Innovation Center of Extreme Optics, Shanxi University, Taiyuan, Shanxi 030006, China*; orcid.org/0000-0002-3131-7559; Email: gyn@pku.edu.cn

**Xiaoyong Hu** − *State Key Laboratory for Artificial Microstructure and Mesoscopic Physics, School of Physics, Peking University, Beijing 100871, China; Frontiers Science Center for Nano-optoelectronics & Collaborative Innovation Center of Quantum Matter, Beijing 100871, China; Collaborative Innovation Center of Extreme Optics, Shanxi University, Taiyuan, Shanxi 030006, China; Beijing Academy of Quantum Information Sciences, Beijing 100193, China*; Email: xiaoyonghu@pku.edu.cn

### Authors

**Yaolong Li** − *State Key Laboratory for Artificial Microstructure and Mesoscopic Physics, School of Physics, Peking University, Beijing 100871, China; Frontiers Science Center for Nano-optoelectronics & Collaborative Innovation Center of Quantum Matter, Beijing 100871, China*

**Wei Liu** − *State Key Laboratory for Artificial Microstructure and Mesoscopic Physics, School of Physics, Peking University, Beijing 100871, China; Frontiers Science Center for Nano-optoelectronics & Collaborative Innovation Center of Quantum Matter, Beijing 100871, China*

**Yunkun Wang** − *State Key Laboratory for Artificial Microstructure and Mesoscopic Physics, School of Physics, Peking University, Beijing 100871, China; Frontiers Science Center for Nano-optoelectronics & Collaborative Innovation Center of Quantum Matter, Beijing 100871, China*

**Zhaohang Xue** − *State Key Laboratory for Artificial Microstructure and Mesoscopic Physics, School of Physics, Peking*




https://dx.doi.org/10.1021/acs.nanolett.0c00742
Nano Lett. 2020, 20, 3747−3753

*University, Beijing 100871, China; Frontiers Science Center for Nano-optoelectronics & Collaborative Innovation Center of Quantum Matter, Beijing 100871, China*

**Yu-Chen Leng** − *State Key Laboratory of Superlattices and Microstructures, Institute of Semiconductors, Chinese Academy of Sciences, Beijing 100083, China*

**Aiqin Hu** − *State Key Laboratory for Artificial Microstructure and Mesoscopic Physics, School of Physics, Peking University, Beijing 100871, China; Frontiers Science Center for Nano-optoelectronics & Collaborative Innovation Center of Quantum Matter, Beijing 100871, China*

**Hong Yang** − *State Key Laboratory for Artificial Microstructure and Mesoscopic Physics, School of Physics, Peking University, Beijing 100871, China; Frontiers Science Center for Nano-optoelectronics & Collaborative Innovation Center of Quantum Matter, Beijing 100871, China; Collaborative Innovation Center of Extreme Optics, Shanxi University, Taiyuan, Shanxi 030006, China; Beijing Academy of Quantum Information Sciences, Beijing 100193, China*

**Ping-Heng Tan** − *State Key Laboratory of Superlattices and Microstructures, Institute of Semiconductors, Chinese Academy of Sciences, Beijing 100083, China;* orcid.org/0000-0001-6575-1516

**Yunquan Liu** − *State Key Laboratory for Artificial Microstructure and Mesoscopic Physics, School of Physics, Peking University, Beijing 100871, China; Frontiers Science Center for Nano-optoelectronics & Collaborative Innovation Center of Quantum Matter, Beijing 100871, China; Collaborative Innovation Center of Extreme Optics, Shanxi University, Taiyuan, Shanxi 030006, China; Beijing Academy of Quantum Information Sciences, Beijing 100193, China*

**Hiroaki Misawa** − *Research Institute for Electronic Science, Hokkaido University, Sapporo 001-0021, Japan; Center for Emergent Functional Matter Science, National Chiao Tung University, Hsinchu 30010, Taiwan;* orcid.org/0000-0003-1070-387X

**Qihuang Gong** − *State Key Laboratory for Artificial Microstructure and Mesoscopic Physics, School of Physics, Peking University, Beijing 100871, China; Frontiers Science Center for Nano-optoelectronics & Collaborative Innovation Center of Quantum Matter, Beijing 100871, China; Collaborative Innovation Center of Extreme Optics, Shanxi University, Taiyuan, Shanxi 030006, China; Beijing Academy of Quantum Information Sciences, Beijing 100193, China*

Complete contact information is available at: https://pubs.acs.org/10.1021/acs.nanolett.0c00742

### Notes

The authors declare no competing financial interest.

## ■ ACKNOWLEDGMENTS

This study was supported by the National Key Research and Development Program of China (2018YFA0704404, 2018YFB2200403, and 2018YFA0306300), National Natural Science Foundation of China (61775003, 11734001, 91950204, 11527901, 91850111, and 11874350), and Beijing Municipal Science and Technology Commission (Z191100007219001). H.M. and Q.S. acknowledge the supports from JSPS KAKENHI (JP18H05205) and Dynamic Alliance for Open Innovation Bridging Human, Environment, and Materials (Five-Star Alliance) of the MEXT. P.T. also acknowledges the support from the CAS Key Research Program of Frontier Sciences (ZDBS-LY-SLH004).

## ■ ABBREVIATIONS

TMDs transition metal dichalcogenides; PEEM photoemission electron microscopy; hBN hexagonal boron nitride; EDCs energy distributions curves; PDMS polydimethylpolysiloxane; AFM atomic force microscopy; LEEM low-energy electron microscopy; OPO optical parametric oscillator

## ■ REFERENCES

(1) Mak, K. F.; Lee, C.; Hone, J.; Shan, J.; Heinz, T. F. Atomically thin $MoS_2$: a new direct-gap semiconductor. *Phys. Rev. Lett.* **2010**, *105*, 136805.

(2) Splendiani, A.; Sun, L.; Zhang, Y.; Li, T.; Kim, J.; Chim, C.-Y.; Galli, G.; Wang, F. Emerging Photoluminescence in Monolayer $MoS_2$. *Nano Lett.* **2010**, *10*, 1271−1275.

(3) Chernikov, A.; Berkelbach, T. C.; Hill, H. M.; Rigosi, A.; Li, Y.; Aslan, O. B.; Reichman, D. R.; Hybertsen, M. S.; Heinz, T. F. Exciton Binding Energy and Nonhydrogenic Rydberg Series in Monolayer $WS_2$. *Phys. Rev. Lett.* **2014**, *113*, 076802.

(4) Liu, H.-L.; Shen, C.-C.; Su, S.-H.; Hsu, C.-L.; Li, M.-Y.; Li, L.-J. Optical properties of monolayer transition metal dichalcogenides probed by spectroscopic ellipsometry. *Appl. Phys. Lett.* **2014**, *105*, 201905.

(5) Zeng, H.; Dai, J.; Yao, W.; Xiao, D.; Cui, X. Valley polarization in $MoS_2$ monolayers by optical pumping. *Nat. Nanotechnol.* **2012**, *7*, 490−493.

(6) Mak, K. F.; He, K.; Shan, J.; Heinz, T. F. Control of valley polarization in monolayer $MoS_2$ by optical helicity. *Nat. Nanotechnol.* **2012**, *7*, 494−498.

(7) Yeh, C.-H.; Chen, H.-C.; Lin, H.-C.; Lin, Y.-C.; Liang, Z.-Y.; Chou, M.-Y.; Suenaga, K.; Chiu, P.-W. Ultrafast Monolayer In/Gr-$WS_2$-Gr Hybrid Photodetectors with High Gain. *ACS Nano* **2019**, *13*, 3269−3279.

(8) Tran, K.; Moody, G.; Wu, F.; Lu, X.; Choi, J.; Kim, K.; Rai, A.; Sanchez, D. A.; Quan, J.; Singh, A.; Embley, J.; Zepeda, A.; Campbell, M.; Autry, T.; Taniguchi, T.; Watanabe, K.; Lu, N.; Banerjee, S. K.; Silverman, K. L.; Kim, S.; Tutuc, E.; Yang, L.; MacDonald, A. H.; Li, X. Evidence for moiré excitons in van der Waals heterostructures. *Nature* **2019**, *567*, 71−75.

(9) Seyler, K. L.; Rivera, P.; Yu, H.; Wilson, N. P.; Ray, E. L.; Mandrus, D. G.; Yan, J.; Yao, W.; Xu, X. Signatures of moiré-trapped valley excitons in $MoSe_2/WSe_2$ heterobilayers. *Nature* **2019**, *567*, 66−70.

(10) Radisavljevic, B.; Radenovic, A.; Brivio, J.; Giacometti, V.; Kis, A. Single-layer $MoS_2$ transistors. *Nat. Nanotechnol.* **2011**, *6*, 147−150.

(11) Lopez-Sanchez, O.; Lembke, D.; Kayci, M.; Radenovic, A.; Kis, A. Ultrasensitive photodetectors based on monolayer $MoS_2$. *Nat. Nanotechnol.* **2013**, *8*, 497−501.

(12) Paik, E. Y.; Zhang, L.; Burg, G. W.; Gogna, R.; Tutuc, E.; Deng, H. Interlayer exciton laser of extended spatial coherence in atomically thin heterostructures. *Nature* **2019**, *576*, 80−84.

(13) Waldecker, L.; Raja, A.; Rösner, M.; Steinke, C.; Bostwick, A.; Koch, R. J.; Jozwiak, C.; Taniguchi, T.; Watanabe, K.; Rotenberg, E.; Wehling, T. O.; Heinz, T. F. Rigid Band Shifts in Two-Dimensional Semiconductors through External Dielectric Screening. *Phys. Rev. Lett.* **2019**, *123*, 206403.

(14) Tongay, S.; Zhou, J.; Ataca, C.; Liu, J.; Kang, J. S.; Matthews, T. S.; You, L.; Li, J.; Grossman, J. C.; Wu, J. Broad-Range Modulation of Light Emission in Two-Dimensional Semiconductors by Molecular Physisorption Gating. *Nano Lett.* **2013**, *13*, 2831−2836.

(15) Lin, Z.; Carvalho, B. R.; Kahn, E.; Lv, R.; Rao, R.; Terrones, H.; Pimenta, M. A.; Terrones, M. Defect engineering of two-dimensional transition metal dichalcogenides. *2D Mater.* **2016**, *3*, 022002.

(16) Zhao, G.-Y.; Deng, H.; Tyree, N.; Guy, M.; Lisfi, A.; Peng, Q.; Yan, J.-A.; Wang, C.; Lan, Y. Recent Progress on Irradiation-Induced Defect Engineering of Two-Dimensional 2H-$MoS_2$ Few Layers. *Appl. Sci.* **2019**, *9*, 678.

(17) Wang, H.; Zhang, C.; Rana, F. Ultrafast Dynamics of Defect-Assisted Electron−Hole Recombination in Monolayer $MoS_2$. *Nano Lett.* **2015**, *15*, 339−345.
(18) Li, L.; Lin, M.-F.; Zhang, X.; Britz, A.; Krishnamoorthy, A.; Ma, R.; Kalia, R. K.; Nakano, A.; Vashishta, P.; Ajayan, P.; Hoffmann, M. C.; Fritz, D. M.; Bergmann, U.; Prezhdo, O. V. Phonon-Suppressed Auger Scattering of Charge Carriers in Defective Two-Dimensional Transition Metal Dichalcogenides. *Nano Lett.* **2019**, *19*, 6078−6086.
(19) Liu, H.; Wang, C.; Zuo, Z.; Liu, D.; Luo, J. Direct Visualization of Exciton Transport in Defective Few-Layer $WS_2$ by Ultrafast Microscopy. *Adv. Mater.* **2020**, *32*, 1906540.
(20) Chen, K.; Ghosh, R.; Meng, X.; Roy, A.; Kim, J.-S.; He, F.; Mason, S. C.; Xu, X.; Lin, J.-F.; Akinwande, D.; Banerjee, S. K.; Wang, Y. Experimental evidence of exciton capture by mid-gap defects in CVD grown monolayer $MoSe_2$. *NPJ. 2D Mater. Appl.* **2017**, *1*, 15.
(21) Docherty, C. J.; Parkinson, P.; Joyce, H. J.; Chiu, M.-H.; Chen, C.-H.; Lee, M.-Y.; Li, L.-J.; Herz, L. M.; Johnston, M. B. Ultrafast Transient Terahertz Conductivity of Monolayer $MoS_2$ and WSe2 Grown by Chemical Vapor Deposition. *ACS Nano* **2014**, *8*, 11147−11153.
(22) Sun, D.; Rao, Y.; Reider, G. A.; Chen, G.; You, Y.; Brézin, L.; Harutyunyan, A. R.; Heinz, T. F. Observation of Rapid Exciton−Exciton Annihilation in Monolayer Molybdenum Disulfide. *Nano Lett.* **2014**, *14*, 5625−5629.
(23) Cunningham, P. D.; McCreary, K. M.; Jonker, B. T. Auger Recombination in Chemical Vapor Deposition-Grown Monolayer $WS_2$. *J. Phys. Chem. Lett.* **2016**, *7*, 5242−5246.
(24) Nie, Z.; Long, R.; Sun, L.; Huang, C.-C.; Zhang, J.; Xiong, Q.; Hewak, D. W.; Shen, Z.; Prezhdo, O. V.; Loh, Z.-H. Ultrafast Carrier Thermalization and Cooling Dynamics in Few-Layer $MoS_2$. *ACS Nano* **2014**, *8*, 10931−10940.
(25) Grubišić Čabo, A.; Miwa, J. A.; Grønborg, S. S.; Riley, J. M.; Johannsen, J. C.; Cacho, C.; Alexander, O.; Chapman, R. T.; Springate, E.; Grioni, M.; Lauritsen, J. V.; King, P. D. C.; Hofmann, P.; Ulstrup, S. Observation of Ultrafast Free Carrier Dynamics in Single Layer $MoS_2$. *Nano Lett.* **2015**, *15*, 5883−5887.
(26) Hein, P.; Stange, A.; Hanff, K.; Yang, L. X.; Rohde, G.; Rossnagel, K.; Bauer, M. Momentum-resolved hot electron dynamics at the 2H-$MoS_2$ surface. *Phys. Rev. B: Condens. Matter Mater. Phys.* **2016**, *94*, 205406.
(27) Wang, L.; Xu, C.; Li, M.-Y.; Li, L.-J.; Loh, Z.-H. Unraveling Spatially Heterogeneous Ultrafast Carrier Dynamics of Single-Layer $WSe_2$ by Femtosecond Time-Resolved Photoemission Electron Microscopy. *Nano Lett.* **2018**, *18*, 5172−5178.
(28) Man, M. K. L.; Margiolakis, A.; Deckoff-Jones, S.; Harada, T.; Wong, E. L.; Krishna, M. B. M.; Madéo, J.; Winchester, A.; Lei, S.; Vajtai, R.; Ajayan, P. M.; Dani, K. M. Imaging the motion of electrons across semiconductor heterojunctions. *Nat. Nanotechnol.* **2017**, *12*, 36−40.
(29) Liu, G.-B.; Shan, W.-Y.; Yao, Y.; Yao, W.; Xiao, D. Three-band tight-binding model for monolayers of group-VIB transition metal dichalcogenides. *Phys. Rev. B: Condens. Matter Mater. Phys.* **2013**, *88*, 085433.
(30) Carvalho, A.; Ribeiro, R. M.; Castro Neto, A. H. Band nesting and the optical response of two-dimensional semiconducting transition metal dichalcogenides. *Phys. Rev. B: Condens. Matter Mater. Phys.* **2013**, *88*, 115205.
(31) Kozawa, D.; Kumar, R.; Carvalho, A.; Kumar Amara, K.; Zhao, W.; Wang, S.; Toh, M.; Ribeiro, R. M.; Castro Neto, A. H.; Matsuda, K.; Eda, G. Photocarrier relaxation pathway in two-dimensional semiconducting transition metal dichalcogenides. *Nat. Commun.* **2014**, *5*, 4543.
(32) Zhang, X.; Qiao, X.-F.; Shi, W.; Wu, J.-B.; Jiang, D.-S.; Tan, P.-H. Phonon and Raman scattering of two-dimensional transition metal dichalcogenides from monolayer, multilayer to bulk material. *Chem. Soc. Rev.* **2015**, *44*, 2757−2785.
(33) Shi, W.; Lin, M.-L.; Tan, Q.-H.; Qiao, X.-F.; Zhang, J.; Tan, P.-H. Raman and photoluminescence spectra of two-dimensional nanocrystallites of monolayer $WS_2$ and $WSe_2$. *2D Mater.* **2016**, *3*, 025016.
(34) McCreary, K. M.; Currie, M.; Hanbicki, A. T.; Chuang, H.-J.; Jonker, B. T. Understanding Variations in Circularly Polarized Photoluminescence in Monolayer Transition Metal Dichalcogenides. *ACS Nano* **2017**, *11*, 7988−7994.
(35) He, Z.; Zhao, R.; Chen, X.; Chen, H.; Zhu, Y.; Su, H.; Huang, S.; Xue, J.; Dai, J.; Cheng, S.; Liu, M.; Wang, X.; Chen, Y. Defect Engineering in Single-Layer $MoS_2$ Using Heavy Ion Irradiation. *ACS Appl. Mater. Interfaces* **2018**, *10*, 42524−42533.
(36) Carozo, V.; Wang, Y.; Fujisawa, K.; Carvalho, B. R.; McCreary, A.; Feng, S.; Lin, Z.; Zhou, C.; Perea-López, N.; Elías, A. L.; Kabius, B.; Crespi, V. H.; Terrones, M. Optical identification of sulfur vacancies: Bound excitons at the edges of monolayer tungsten disulfide. *Sci. Adv.* **2017**, *3*, No. e1602813.
(37) Schuler, B.; Lee, J.-H.; Kastl, C.; Cochrane, K. A.; Chen, C. T.; Refaely-Abramson, S.; Yuan, S.; van Veen, E.; Roldán, R.; Borys, N. J.; Koch, R. J.; Aloni, S.; Schwartzberg, A. M.; Ogletree, D. F.; Neaton, J. B.; Weber-Bargioni, A. How Substitutional Point Defects in Two-Dimensional $WS_2$ Induce Charge Localization, Spin−Orbit Splitting, and Strain. *ACS Nano* **2019**, *13*, 10520−10534.
(38) Shi, W.; Zhang, X.; Li, X.-L.; Qiao, X.-F.; Wu, J.-B.; Zhang, J.; Tan, P.-H. Phonon Confinement Effect in Two-dimensional Nanocrystallites of Monolayer $MoS_2$ to Probe Phonon Dispersion Trends Away from Brillouin-Zone Center. *Chin. Phys. Lett.* **2016**, *33*, 057801.
(39) Chow, P. K.; Jacobs-Gedrim, R. B.; Gao, J.; Lu, T.-M.; Yu, B.; Terrones, H.; Koratkar, N. Defect-Induced Photoluminescence in Monolayer Semiconducting Transition Metal Dichalcogenides. *ACS Nano* **2015**, *9*, 1520−1527.
(40) Castellanos-Gomez, A.; Buscema, M.; Molenaar, R.; Singh, V.; Janssen, L.; van der Zant, H. S. J.; Steele, G. A. Deterministic transfer of two-dimensional materials by all-dry viscoelastic stamping. *2D Mater.* **2014**, *1*, 011002.


https://dx.doi.org/10.1021/acs.nanolett.0c00742
*Nano Lett.* 2020, 20, 3747−3753

# Supporting Information

# Ultrafast Electron Cooling and Decay in Monolayer $WS_2$ Revealed by Time- and Energy-Resolved Photoemission Electron Microscopy

*Yaolong Li,[†,‡] Wei Liu,[†,‡] Yunkun Wang,[†,‡] Zhaohang Xue,[†,‡] Yu-Chen Leng,[#] Aiqin Hu,[†,‡] Hong Yang,[†,‡,§,∥] Ping-Heng Tan,[#] Yunquan Liu,[†,‡,§,∥] Hiroaki Misawa,[⊥,▽] Quan Sun,[⊥,*] Yunan Gao,[†,‡,§,*] Xiaoyong Hu,[†,‡,§,∥,*] and Qihuang Gong[†,‡,§,∥]*

[†]State Key Laboratory for Artificial Microstructure and Mesoscopic Physics, School of Physics, Peking University, Beijing 100871, China

[‡]Frontiers Science Center for Nano-optoelectronics & Collaborative Innovation Center of Quantum Matter, Beijing 100871, China

[§]Collaborative Innovation Center of Extreme Optics, Shanxi University, Taiyuan, Shanxi 030006, China

[∥]Beijing Academy of Quantum Information Sciences, Beijing 100193, China

[#]State Key Laboratory of Superlattices and Microstructures, Institute of Semiconductors, Chinese Academy of Sciences, Beijing 100083, China

[⊥]Research Institute for Electronic Science, Hokkaido University, Sapporo 001–0021, Japan

[▽]Center for Emergent Functional Matter Science, National Chiao Tung University, Hsinchu 30010, Taiwan

**Table of Contents:**

**1. AFM image of the supported $WS_2$**

**2. PL and Raman characterizations**

**3. FDTD simulations on optical interference effect**

**4. Time resolution of the TR-PEEM measurements**

**5. PEEM measurements for the supported $WS_2$**

**6. PEEM measurements for the suspended $WS_2$**

**7. Movie of TR-PEEM signals for the supported $WS_2$**

## 1. AFM image of the supported $WS_2$

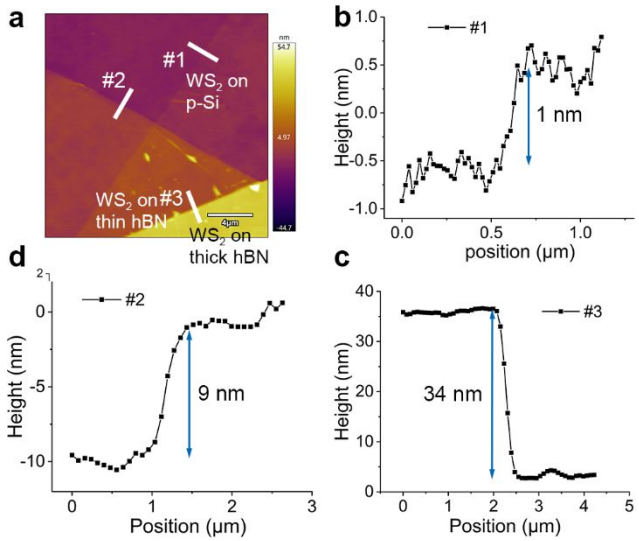


**Figure S1**. (a) AFM image of the supported monolayer $WS_2$ on p-Si and hBN (by Cypher VRS, Oxford Instruments). (b-c) Crosscuts from (a). The $WS_2$ was verified to be monolayer. The thicknesses of thin and thick hBN flakes are about 9 nm and 43 nm (9 nm + 34 nm), respectively.

## 2. PL and Raman characterizations

We measured the photoluminescence (PL) and Raman spectra to characterize the optical properties and sample quality.

The PL spectra were measured at room temperature using a continuous 532 nm laser, and an

inverted microscope (Eclipse Ti-2 inverted microscope, Nikon) equipped with an objective lens (40×, NA = 0.6) and a spectrometer (Kymera 328i, Andor). The PL intensities are totally quenched on all the three regions for the supported $WS_2$ after PEEM measurements (Figure S2a). In contrast, the PL intensity is significantly strong even with much weaker excitation laser for the pristine $WS_2$ on PDMS (Figure S2b). The PL mapping of the suspended $WS_2$ after PEEM measurements and the extracted PL spectra along a yellow dashed line are shown in Figure S2c,d, in which the intensity variations across the hole are determined by both the optical interference effect induced by the underlying hole, and local defect density introduced during PEEM measurements. The PL intensity is also strongly quenched for the suspended $WS_2$ but still measurable, and the two peaks of PL spectra are attributed to A exciton (615 nm, 2.02 eV) and defect-bound exciton (~ 660 nm, 1.88 eV) (Figure S2e). Therefore, the PL spectra indicate the presence of defects on the supported and suspended $WS_2$ after PEEM measurements.

In order to avoid possible contamination during PL measurements, we didn't measure the PL spectra for the sample with $WS_2$ on hBN/Si investigated in the main text prior to PEEM measurements. Instead, we have measured PL spectra for other samples with monolayer $WS_2$ on Si and hBN following the same fabrication process. Figure S3 shows the PL spectra for samples of monolayer $WS_2$ on hBN/Si and on PDMS. As shown in Figure S3a and the inset of Figure S3c, the PL intensity for $WS_2$ on hBN/Si is weaker than on PDMS, probably due to the optical interference effect, as discussed by several publications.[1, 2] The peak shifts for $WS_2$ on different substrates, as shown in Figure S3c, are due to the difference in dielectric environment.[3]

The Raman spectra were measured at room temperature using a Jobin-Yvon HR800 micro-Raman system, equipped with a liquid-nitrogen-cooled charge couple detector (CCD) and an objective lens (100×, NA = 0.90). The laser excitation wavelength was 488 nm from an $Ar^+$ laser. The 1800 lines/mm grating was used in the Raman measurements, which enabled each CCD pixel to cover 0.62$cm^{-1}$ at 488nm. A low laser power of 80 μW was used to avoid heating and damaging. The Raman spectra for the supported and suspended $WS_2$ after PEEM measurements and another pristine $WS_2$ on PDMS are shown in Figure 3c and Figure S4. It

should be noted that, for the supported $WS_2$, we measured the Raman spectra for $WS_2$ on the 43-nm hBN only, considering that the Raman signal could be very weak for $WS_2$ directly on p-Si because of the lack of Raman enhancement effect by optical interference.[2, 4]

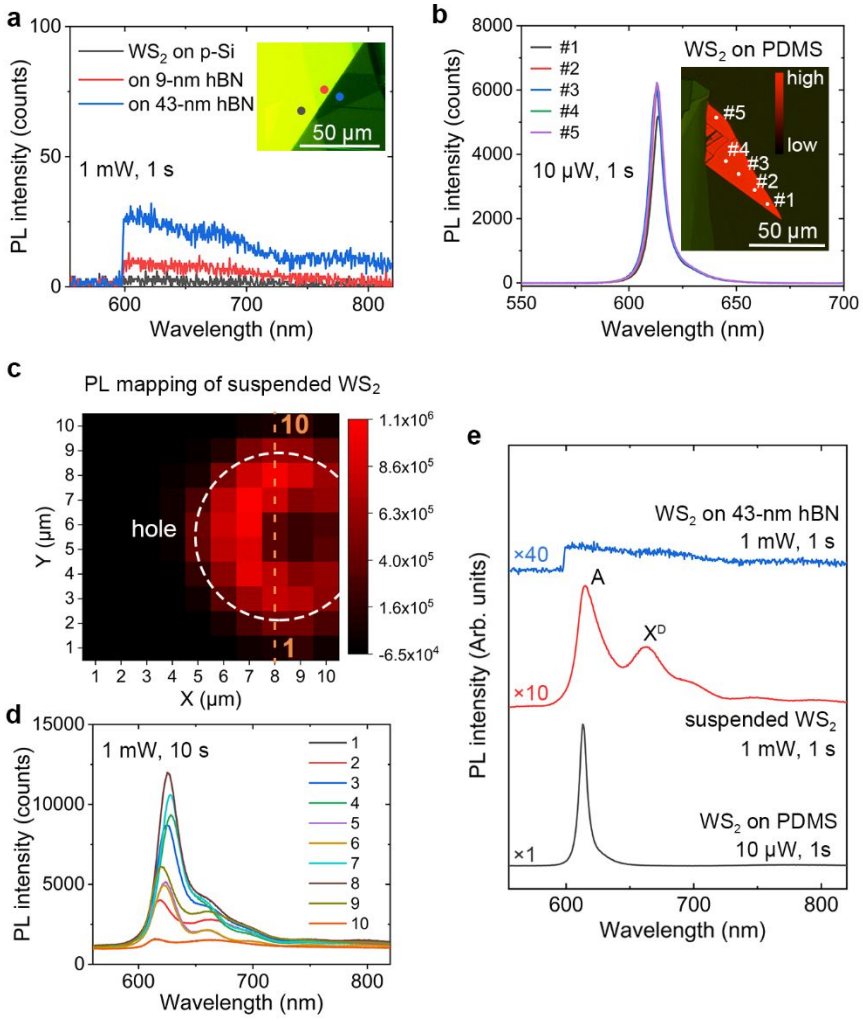


**Figure S2**. PL spectra for the supported and suspended $WS_2$ after PEEM measurements and the pristine $WS_2$ on PDMS. The power of excitation laser, and integration time are labeled. (a) PL spectra for the supported $WS_2$. (b) PL spectra for the pristine $WS_2$. (c) PL mapping of the suspended $WS_2$, and the spectra along the crosscut are shown in (d). (e) Comparison of PL spectra.

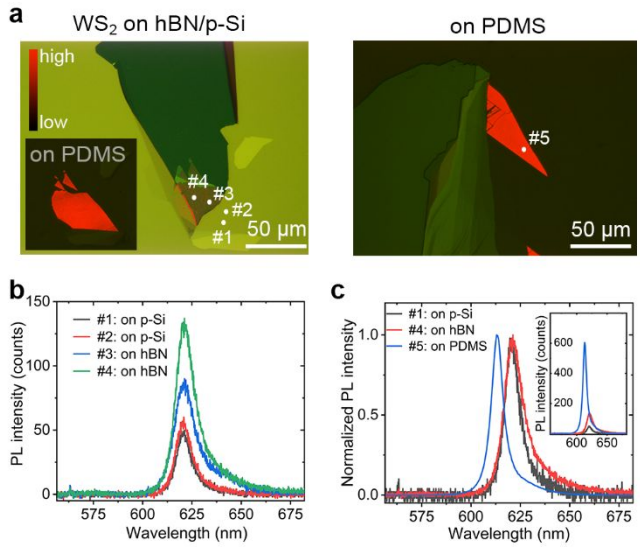


**Figure S3**. (a) Optical microscopy images (showing PL signals) for samples of monolayer $WS_2$ on hBN/Si and on PDMS without PEEM measurements. The inset in the left corner shows the image for the $WS_2$ before transferred to hBN/p-Si. (b) PL spectra for $WS_2$ on hBN/p-Si. (c) Comparison of the PL spectra. The PL spectra were measured with 532 nm CW laser with power of 1 μW and acquisition time of 1 s.

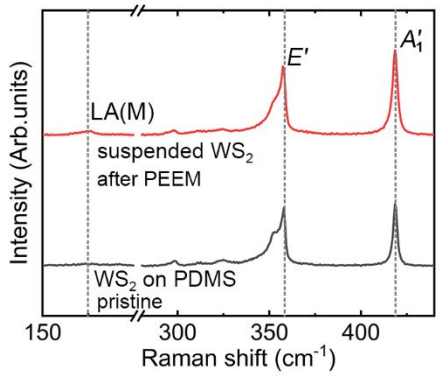


**Figure S4**. Raman spectra for the suspended $WS_2$ after PEEM measurements and the pristine $WS_2$ on PDMS.

The passivation of S-vacancy by oxygen adsorption has been reported by Nan et al.[5] Such a passivation mechanism can be enhanced by laser illumination in ambient condition, as reported in Ref.,[6, 7] the monolayer $WS_2$ or $MoS_2$ were found to exhibit considerable enhancement in the PL intensity after the laser treatments. They demonstrated that the enhancement arises from the healing of defects in monolayers via adsorption or substitution of the sulfur vacancies with oxygen. In our study, we observed a slight enhancement of PL intensity with laser treatment in

ambient condition for the monolayer $WS_2$ after PEEM measurements. Therefore, we speculate the PEEM measurement induced defects are of S-vacancies. As shown in Figure S5, the PL intensities were enhanced for the suspended $WS_2$ and another $WS_2$ samples after PEEM measurements during the PL measurements. Classification of defect types and the formation mechanism might need much more efforts to investigate in the future.

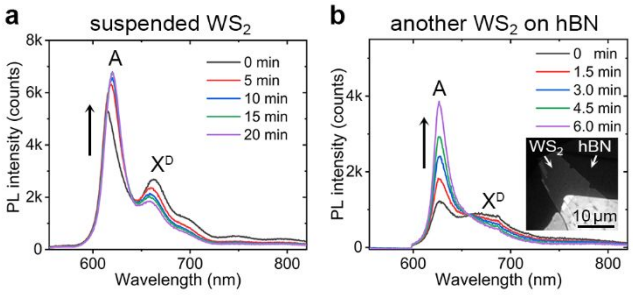


**Figure S5**. Enhancement of PL intensity with laser illumination time in ambient condition for monolayer $WS_2$ after PEEM measurements. (a) The suspended $WS_2$ investigated in the main text. (b) Another $WS_2$ sample on hBN after PEEM measurements (not shown in the main text), the PEEM image with excitation wavelengths of 410 nm (15 μJ/cm$^2$) is shown as inset. The laser setup was the same as other PL measurements, and the laser was 532 nm CW laser with power of about 1 mW for (a) and 0.5 mW for (b) with spot diameter of 1~2 mm.

We have samples prepared with the same method and kept in the preparation chamber of PEEM (approximately $10^{-9}$ Torr) for ~24 h without laser illumination, and found that the PL intensity was strong and no defect-related peak could be observed. Figure S6 shows the PL spectrum for $WS_2$ on hBN/20 nm $SiO_2$/Si after this treatment. The PL intensity is comparable to that in Figure S3b, and the lower shoulder at ~638 nm is from trions. This measurement excluded the possibility of slow dark degradation of the sample in ultra-high vacuum. The degradation could be a combined effect, and the mechanism is not clarified yet.

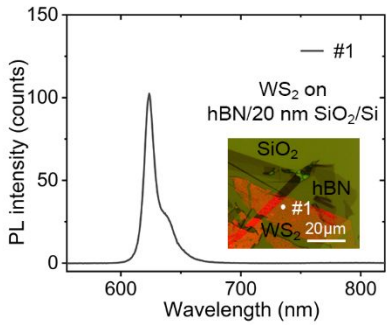


**Figure S6**. PL spectrum for $WS_2$ on hBN/20 nm $SiO_2$/Si substrate (1 μW, 1 s). The two peaks are attributed to excitons and trions, respectively. The sample was kept in the preparation chamber of PEEM (approximately $10^{-9}$ Torr) for ~24 h without laser illumination.

### 3. FDTD simulations on optical interference effect

To understand the experimental large contrast of PE intensity for the supported $WS_2$ on the three different regions of p-Si, 9-nm and 43-nm hBN, we simulated the near-field intensity on monolayer $WS_2$ with finite-difference time-domain (FDTD) solutions (Lumerical FDTD solutions) using the structure shown in Figure S7a, which is a typical film-interference structure. The refractive index of $WS_2$ was adopted from literature[8] and the thickness was set as 0.8 nm. The refractive index of hBN was set as 2.1.[4] The thickness of native $SiO_2$ layer on p-Si was set as 2 nm. The simulated electric field intensity $|E|^2$ as a function of hBN thickness and wavelength is shown in Figure S7b. The extracted $|E|^2$ for wavelengths of 273 nm and 410 nm are shown in Figure S7c, in which the intensities vary periodically with hBN thickness. By comparing the simulations with experiments, the large contract of PE intensity is strongly correlated to optical interference effect. The quantitative difference between simulations and experiments was probably due to the parameter used in simulations, e.g. refractive index of hBN, and PE nonlinear order of $WS_2$. The underlying substrate could also possibly modify the PE efficiency of $WS_2$. In addition, the optical interference effect can also be clearly observed on the suspended $WS_2$, as shown in Figure S14.

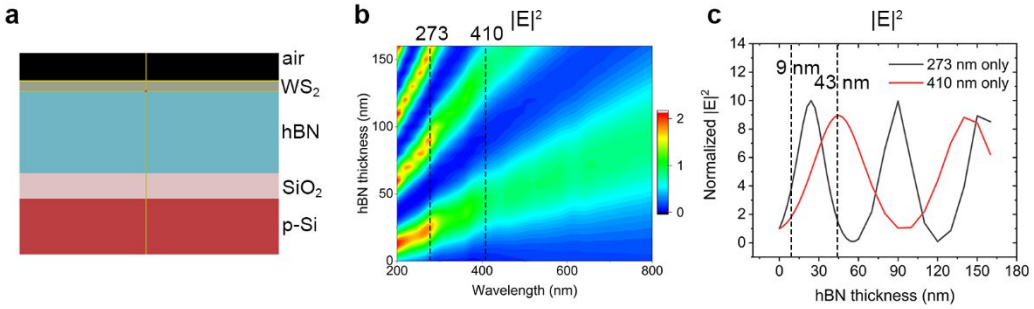


**Figure S7**. (a) Designed structure for FDTD simulations. (b) Mapping of electric field intensity $|E|^2$ versus wavelength and hBN thickness. (c) Simulated electric field intensity of $|E|^2$ on $WS_2$ layer as a function of hBN thickness for wavelengths of 273 nm and 410 nm, normalized by the intensity without hBN layer.

## 4. Time resolution of the TR-PEEM measurements

The time resolution of the TR-PEEM system was evaluated by using the cross-correlation signals observed on the p-Si substrate during the pump–probe measurements. As shown in Figure S8a, a sharp peak was observed at the pump wavelength of 590 nm directly on the p-Si substrate. The sharp peak on the p-Si substrate was attributed to the cross-correlation signals between the pump and probe pulses because the following PE intensity was still increasing, which could be attributed to the slowly increased pump–probe signals on the p-Si. Similar to the intensity autocorrelation measurement, the cross-correlation measurement can be used to obtain the time resolution of the pump–probe system. Assuming Gaussian-shaped pump and probe pulses with intensities of $I_1(t)$ and $I_2(t)$, the PE intensity induced by the cross correlation can be expressed as

$$PE(t) \propto \int_{\infty}^{\infty} I_1(t) I_2(t-\tau) d\tau = \frac{1}{\sqrt{2\pi(\sigma_1^2+\sigma_2^2)}} \exp\left[-\frac{(t-\Delta t)^2}{2(\sigma_1^2+\sigma_2^2)}\right], \quad \text{(S1)}$$

where $\Delta t$ is the time delay between the pump and probe pulses and $\sigma_1$ and $\sigma_2$ are related to the durations of the two pulses. The fitted Gaussian-shaped PE intensity is shown in Figure S8b, which can be used to obtain the full width at half maximum (FWHM). Similar to the relation between the intensity autocorrelation width and pulse duration, the time resolution of our system was $1/\sqrt{2}$ of the FWHM of the cross-correlation signal (approximately 200 fs). The time resolutions with other pump wavelengths were similar to this value.

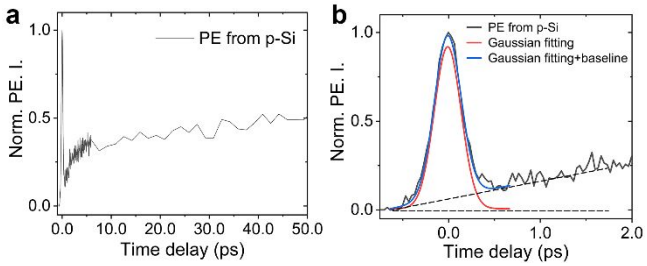


**Figure S8**. (a) Normalized TR-PEEM signal directly on the p-Si substrate (without $WS_2$) with the excitation wavelength of 590 nm. (b) Enlarged view of the peak in (a), Gaussian fitting of the

peak (red line), and that with added baseline (blue line) to compare with the experimental data.

## 5. PEEM measurements for the supported $WS_2$

The PE signals are dominantly from monolayer $WS_2$. As shown in Figure S9, the PE intensity from p-Si (no $WS_2$) is much weaker than that from $WS_2$ on p-Si and on hBN. Furthermore, the PE intensity is very sensitive to surface, the PE intensity from p-Si underneath $WS_2$ layer will be much weaker than that without $WS_2$. Therefore, the signal from the underlying p-Si are negligible. In addition, the normalized PE intensity traces are independent of the pump fluence, as shown in Figure S10.

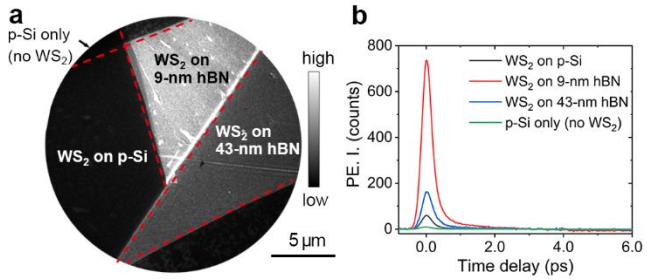


**Figure S9**. (a) PEEM image at pump–probe zero-time delay with the pump pulse 410 nm (15 μJ/cm$^2$) and the probe pulse 273 nm (0.5 μJ/cm$^2$). (b) PE intensity traces on different regions.

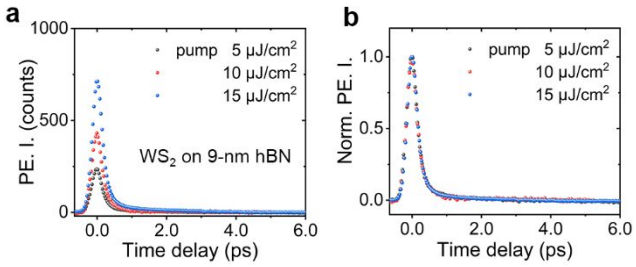


**Figure S10**. PE intensity traces (a) and the normalized ones (b) with different pump fluences for $WS_2$ on 9-nm hBN.

The evolutions of electron energy distribution in time, for $WS_2$ on the three regions with the pump wavelength of 410 nm, are shown in Figure S11a–c. The fluences of pump and probe pulses were 10 μJ/cm$^2$ and 0.5 μJ/cm$^2$, respectively. The EDCs at 0-ps time delay are shown in Figure S11d,e. Despite the large difference in PE intensity for $WS_2$ on different regions, the EDCs after normalization are similar, and the differences among different regions are comparable to energy resolution of around 150 meV. It should be noted the EDCs discussed

above were obtained by subtracting the background signals before pump–probe zero point. The contribution from secondary electrons should be weakened or eliminated under this operation. Therefore, the EDCs are dominated by pump–probe signals, which represent the populations of photoexcited electrons in conduction band. However, we are not sure if the Auger processes, surface photovoltage effects or in-gap defects have some contributions to the cutoff of EDCs. It should be noted that, the transition from non-equilibrium distribution to hot electron distribution has been demonstrated to be ultrafast (tens of femtoseconds), much shorter than the excitation pulse duration of 120 fs. In addition, we assign the moment with peak PE intensity to the 0-ps time delay, which could be slightly later than the real pump–probe overlapping point, because the number of thermalized electrons in the PE detection window could be larger than that at the instant of photoexcitation due to the electron-electron and electron-photon scattering. Considering the asymmetric EDC at 0-ps time delay, the hot electron distribution should have been formed.

The trap states could be highly localized in real space and delocalized in reciprocal space, and could be within the PE detection window shown in Figure 3 of the main text. However, no signal from the trap states were observed in the EDCs, which implies that the PE efficiency of electrons from trap states are much lower than that from conduction bands.

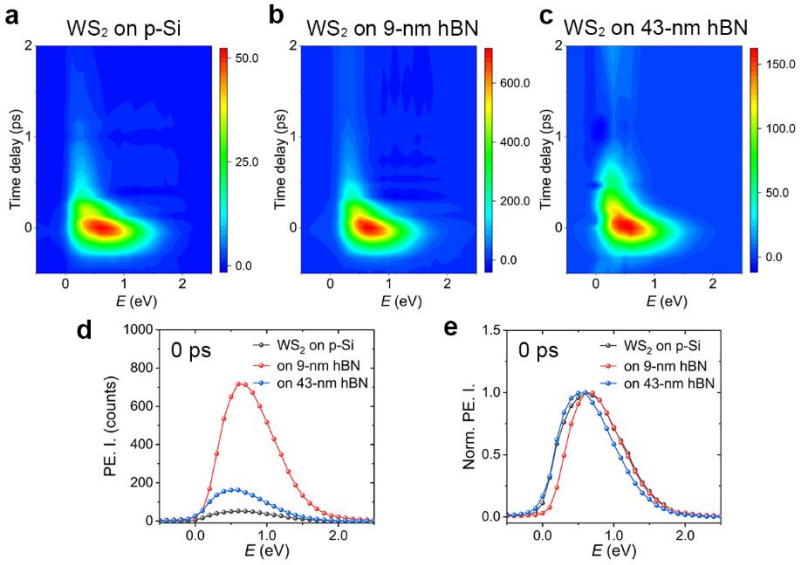


**Figure S11.** (a–c) Mapping of the PE intensity versus the energy and time delay for the $WS_2$ on

the three regions with the pump wavelength of 410 nm. The EDCs at 0-ps time delay and the normalized EDCs are shown in (d,e).

We also performed TR-PEEM measurements with other pump wavelengths, e.g. 590 nm, by using OPO. More importantly, we noticed the change of decay traces with the accumulated measurement time, as shown in Figure S12. The decay time decreases slowly with PEEM measurement days, indicating the increase of defects at a slow rate, and such a slow rate is possibly due to the low laser fluences.

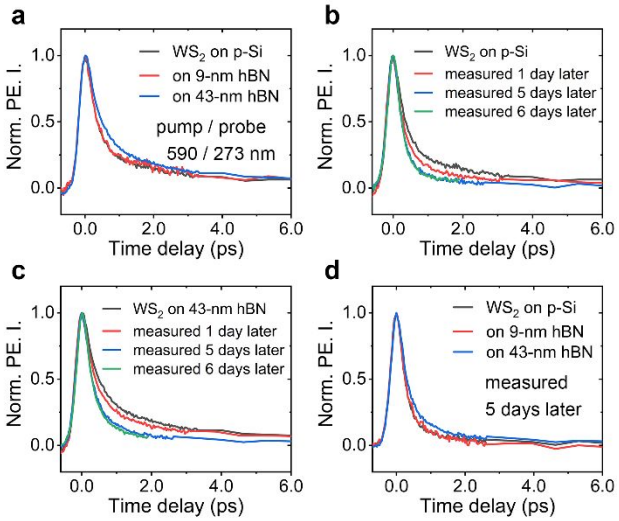


**Figure S12**. (a) Normalized PE intensity traces for $WS_2$ on the three regions with the pump wavelength of 590 nm. (b,c) Decay traces measured at different days for $WS_2$ on p-Si and 43-nm hBN, respectively. (d) Decay traces measured 5 days later than that in (a). The decay time decreases slowly with PEEM measurement days, indicating the increase of defects with laser illumination at a slow rate.

We also performed the time- and energy-resolved PEEM measurements with the pump wavelength of 590 nm, as shown Figure S13. The trend of EDCs is similar as that with the pump wavelength of 410 nm, except that the populations in energy are lower owing to the lower photon energy. In addition, the EDCs with pump wavelengths of 590 nm and 410 nm have the same cutoff edge. The EDCs were also fitted with Fermi–Dirac distribution as discussed in the main text. It should be noted that the fitting method is not so strict, since the real density of states was not adopted. The density of states was simplified as the form of square root, considering the

increasing tendency of density of states with energy and the limited PE detection window.

It should be noted that, in our energy-resolved PEEM experiments, we can only obtain the relative values of photoemitted electron energy from the energy analyzer. That is to say, we could obtain the EDCs but not knowing the absolute electron energy. We found that the cutoff edge of different EDCs obtained with different pump wavelengths and from different sample regions are nearly at identical energy. Hence, we set the cutoff edge in the energy axis of EDCs to be energy zero. Considering the band diagram of $WS_2$ as shown in Figure 3 of the main text, the energy zero is likely at the conduction band edge of Q valley (lowest energy in the PE detection window).

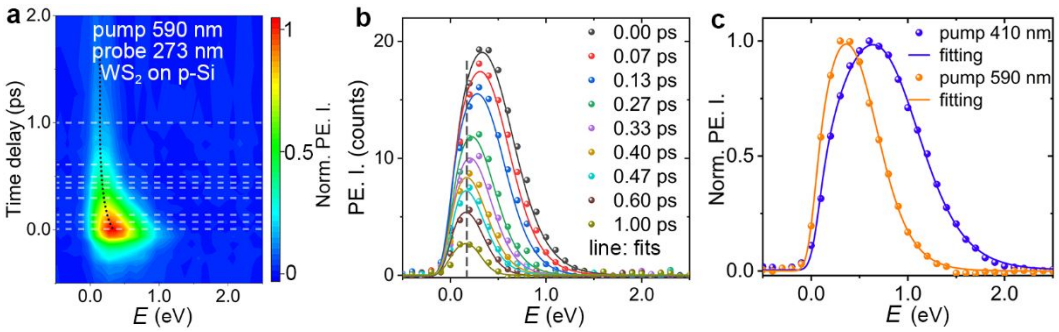


**Figure S13.** (a) Mapping of the PE intensity versus the energy and time delay for the $WS_2$ on the p-Si with the pump wavelength of 590 nm. (b) Crosscuts from (a) and fittings of the EDCs with Fermi–Dirac distributions. (c) Comparison of the EDCs at 0-ps time delay with the pump wavelengths of 410 and 590 nm, the electronic temperature with 590 nm (1900 K) is approximately 900 K lower than that with 410 nm (2800 K).

## 6. PEEM measurements for the suspended $WS_2$

The static PEEM images with different excitation wavelengths and incident angles are shown in Figure S14. The bright spot could be seen with the excitation wavelength of 410 nm at normal incidence, as shown in Figure S14b,e. To eliminate the bright spot, we used oblique incidence with s-polarization, as shown in Figure S14c,f, in which the interference patterns are observed. However, the decay traces with the normal and oblique incidences overlap well, proving that the carrier dynamics are independent of pump fluence, but correlated to defects introduced slowly by

accumulated laser illumination. We performed TR-PEEM measurements at normal incidence with different pump fluences, also showing that the decay time is not sensitive to pump fluence, as shown in Figure S15.

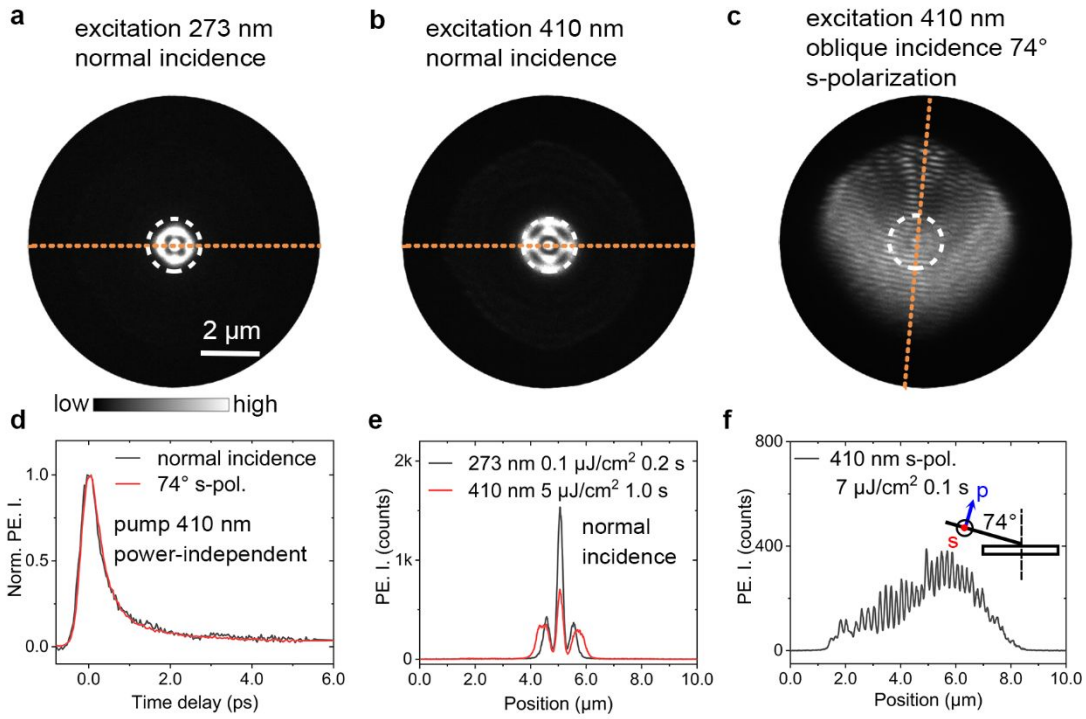


**Figure S14.** (a,b) Static PEEM images with excitation wavelengths of 273 nm (0.1 μJ/cm$^2$) and 410 nm (5 μJ/cm$^2$), respectively, at normal incidence. The crosscuts along the yellow line are shown in (e). (c) Static PEEM image with the excitation wavelength of 410 nm (7 μJ/cm$^2$) at oblique incidence of 74°, with s-polarization. The crosscut along the yellow line is shown in (f). (d) Decay traces extracted from the central region (marked by white dashed circle) with the pump wavelength of 410 nm at normal and oblique incidences, indicating the carrier dynamics are independent of pump fluence.

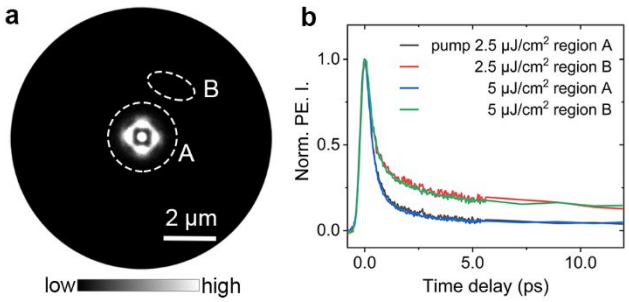


**Figure S15.** (a) TR-PEEM image with the pump pulse 410 nm (5 μJ/cm$^2$) and the probe pulse 273 nm (0.1 μJ/cm$^2$) at 0-ps time delay. (b) Decay traces with pump fluences of 2.5 μJ/cm$^2$ and 5

μJ/cm$^2$ on the two regions marked in (a).

We did the probe–fluence dependence experiment, with the similar method for pump fluence, as shown in Figure S16, proving that the carrier dynamics are also independent of probe fluence in a short time.

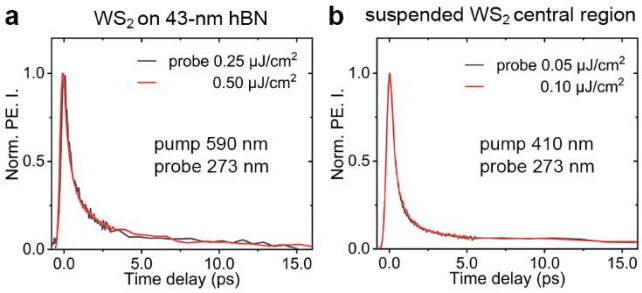


**Figure S16**. Normalized PE intensity traces with different probe fluences for $WS_2$ on 43-nm hBN (a) and suspended $WS_2$ in the central region (b). The pump pulses were set as 590 nm (19 μJ/cm$^2$) in (a) and 410 nm (5 μJ/cm$^2$) in (b).

## 7. Movie of TR-PEEM signals for the supported $WS_2$

The movie shows pump–probe PEEM signals at a series of time delays with the pump pulse 410 nm (10 μJ/cm$^2$) and the probe pulse 273 nm (0.5 μJ/cm$^2$) at normal incidence.

REFERENCES

(1). Lien, D.-H.; Kang, J. S.; Amani, M.; Chen, K.; Tosun, M.; Wang, H.-P.; Roy, T.; Eggleston, M. S.; Wu, M. C.; Dubey, M.; Lee, S.-C.; He, J.-H.; Javey, A., Engineering Light Outcoupling in 2D Materials. *Nano Lett.* **2015,** *15*, 1356–1361.

(2). Yoon, D.; Moon, H.; Son, Y.-W.; Choi, J. S.; Park, B. H.; Cha, Y. H.; Kim, Y. D.; Cheong, H., Interference effect on Raman spectrum of graphene on $SiO_2$/Si. *Phys. Rev. B* **2009,** *80*, 125422.

(3). Raja, A.; Chaves, A.; Yu, J.; Arefe, G.; Hill, H. M.; Rigosi, A. F.; Berkelbach, T. C.; Nagler, P.; Schüller, C.; Korn, T.; Nuckolls, C.; Hone, J.; Brus, L. E.; Heinz, T. F.; Reichman, D. R.; Chernikov, A., Coulomb engineering of the bandgap and excitons in two-dimensional materials. *Nat. Commun.* **2017,** *8*, 15251.

(4). Lee, S.-Y.; Jeong, T.-Y.; Jung, S.; Yee, K.-J., Refractive Index Dispersion of Hexagonal Boron Nitride in the Visible and Near-Infrared. *Phys. Status Solidi (b)* **2019,** *256*, 1800417.

(5). Nan, H.; Wang, Z.; Wang, W.; Liang, Z.; Lu, Y.; Chen, Q.; He, D.; Tan, P.; Miao, F.; Wang, X.; Wang, J.; Ni, Z., Strong Photoluminescence Enhancement of $MoS_2$ through Defect Engineering and Oxygen Bonding. *ACS Nano* **2014,** *8*, 5738–5745.

(6). Venkatakrishnan, A.; Chua, H.; Tan, P.; Hu, Z.; Liu, H.; Liu, Y.; Carvalho, A.; Lu, J.; Sow, C. H., Microsteganography on $WS_2$ Monolayers Tailored by Direct Laser Painting. *ACS Nano* **2017,** *11*, 713–720.

(7). Ardekani, H.; Younts, R.; Yu, Y.; Cao, L.; Gundogdu, K., Reversible Photoluminescence Tuning by Defect Passivation via Laser Irradiation on Aged Monolayer $MoS_2$. *ACS Appl. Mater. Interfaces* **2019,** *11*, 38240–38246.

(8). Jung, G.-H.; Yoo, S.; Park, Q.-H., Measuring the optical permittivity of two-dimensional materials without a priori knowledge of electronic transitions. *Nanophotonics* **2018,** *8*, 263–270.